Experimental characterisation of the screech feedback loop in underexpanded round jets

Bertrand Mercier[1,†], Thomas Castelain[2] and Christophe Bailly[1]

[1]Université de Lyon, Ecole Centrale de Lyon and LMFA UMR CNRS 5509, F-69134 Ecully, France

[2]Université de Lyon, Université Lyon 1 and LMFA UMR CNRS 5509, F-69622 Villeurbanne, France

Near-field acoustic measurements and time-resolved schlieren visualisations are performed on 10 round jets with the aim of analysing the different parts of the feedback loop related to the screech phenomenon in a systematic fashion. The ideally expanded Mach number of the studied jets ranges from $M_j = 1.07$ to $M_j = 1.50$. The single source of screech acoustic waves is found at the fourth shock tip for A1 and A2 modes, and at either the third or the fourth shock tip for the B mode, depending on the Mach number. The phase of the screech cycle is measured throughout schlieren visualisations in the shear layer from the nozzle to the source. Estimates of the convective velocities are deduced for each case, and a trend for the convective velocity to grow with the axial distance is pointed out. These results are used together with source localisation deduced from a two-microphone survey to determine the number of screech periods contained in a screech loop. For the A1 and B modes, four periods are contained in a loop for cases in which the radiating shock is the fourth, and three periods when the radiating shock tip is the third, whereas the loop of the A2 mode contains five periods.

Key words: acoustics, aeroacoustics, jet noise

---

1. Introduction

Noise produced by imperfectly expanded supersonic jets differs from subsonic jet noise by the emergence of shock noise. Major knowledge about supersonic jet noise is available in comprehensive reviews, for example in Tam (1995), Raman (1999) or Bailly & Fuji (2016). The present paper focuses on the screech, a strong tonal contribution of shock noise. Attention will be paid particularly to the structure of the resonant loop sustaining this phenomenon. One mechanism of screech tone generation was first proposed by Powell (1953), and has been the subject of many studies until the present day. Powell observed the staging behaviour of the screech frequencies produced by round jets, and identified four modes: A, B, C and D. Mode A was later separated into A1 and A2 by Merle (1957) after investigation based on stroboscopic schlieren visualisation. Davies & Oldfield (1962) have shown using two microphones on either side of the jet that the A1 and A2 modes are axisymmetric, whereas the B

and C modes are helical. The B and D modes were later recognised as flapping in nature by Powell, Umeda & Ishii (1992) and by Ponton & Seiner (1995), who carried out a survey with 10 microphones distributed around the jet. Ponton & Seiner (1995) found that the B and D modes comprise two oppositely rotating helices.

Theoretical knowledge about screech tone generation was supported by the model of a resonant loop developed by Powell (1953), which predicts the screech frequency f_s as a function of the convective velocity U_c of the turbulent structures, the shock cell length L_{sc} and the ambient speed of sound c_0:

$$f_s = \frac{U_c}{L_{sc}(1 + U_c/c_0)}. \tag{1.1}$$

Harper-Bourne & Fisher (1973) considered an array of equally spaced sources distributed along the lip line. The sources are shifted in phase by a lag corresponding to the time spent by the structures to be convected between two consecutive sources. By assuming that all the sound waves interfere constructively at the nozzle exit, a necessary condition on screech frequency to enhance the feedback loop was obtained, identical to (1.1). Later, Tam, Seiner & Yu (1986) derived the same equation for f_s by considering the upstream propagating wave produced by the interaction between the periodic shock cell pattern and an instability wave. Powell, Umeda & Ishii (1990) revised his model by including a phase lag to take into account the phase changes at the source or nozzle interactions, but this correction does not seem to be widely used.

Powell *et al.* (1992) observed by means of schlieren visualisations that the acoustic feedback emanated from a single source. Umeda & Ishii (2001) and Tam, Parrish & Viswanathan (2014) conducted similar schlieren visualisations that also led them to observe a single source. Suzuki & Lele (2003) performed a direct numerical simulation of a problem representative of an underexpanded jet shear layer. They observed that the passage of an eddy at a shock position may cause the shock to leak out from the mixing layer. Shariff & Manning (2013) observed the same phenomenon from a ray tracing study. Shock leakage has also been recognised as being the screech acoustic feedback generation mechanism by Berland, Bogey & Bailly (2007) by means of a large-eddy simulation of a planar jet. Based on unsteady Reynolds-averaged Navier–Stokes simulations, Gao & Li (2010) proposed a generalisation of (1.1) considering a unique source by introducing three parameters: the number of shock cells N between the nozzle and the source, the total number of wavelengths m involved in the screech loop and the convective velocity U_c:

$$f_s = \frac{mU_c}{NL_{sc}(1 + U_c/c_0)}. \tag{1.2}$$

In this model as well as in (1.1), the staging behaviour of screech tones is not accounted for. To overcome this problem, Gao & Li (2010) characterised each mode by a specific set of parameters m and N, and by the ratio of convective velocity to jet velocity. The latter is the only variable in (1.1). This ratio U_c/U_j, where U_j is the jet exhaust velocity of an equivalent perfectly expanded jet, is in general found to be between 0.55 and 0.7 (Powell *et al.* 1992; Panda 1996; Massey & Ahuja 1997; Gao & Li 2010). Nonetheless, keeping U_c/U_j constant for a given mode requires the ratio to be independent of the Mach number and constant along the jet shear layer. This statement is in contradiction with measurements performed four diameters downstream of the nozzle in jet shear layers by Veltin & McLaughlin (2008). They observed a dependence of the convective velocity on Mach number,

Reference	Source location	Mode considered	Method
Powell *et al.* (1992)	$z \simeq 5D$	A1, A2, B	Schlieren
Powell *et al.* (1992)	$z \simeq 6D$	C	Schlieren
Umeda & Ishii (2001)	Rear edge of 3rd s.c.	A1, B, C	Schlieren
Tam *et al.* (2014)	5–6 s.c. downstream	$M_j = 1.58, M_d = 2.0$	Schlieren
Panda (1999)	Between 3rd and 4th tip	A2	Acoustics
Gao & Li (2010)	Between 2nd and 4th s.c.	A1, A2, B, C	CAA
Edgington-Mitchell *et al.* (2014)	Between 2nd and 4th s.c.	C	PIV

TABLE 1. Localisation of screech source for circular jets: s.c. = shock cell; CAA = computational aeroacoustics; PIV = particle image velocimetry.

resulting in variation of U_c/U_j from 0.7 at $M_j = 1$ to 0.57 at $M_j = 1.56$, where M_j is the equivalent ideally expanded jet Mach number. A spatial dependence was also pointed out by Gojon, Bogey & Marsden (2015), who reported from a numerical simulation that the convective velocity increases with the downstream distance z from the nozzle. Equation (1.1) also requires that the shock cell length be constant, whereas it decreases with the axial distance from the nozzle exit z (Tam, Jackson & Seiner 1985; Tam *et al.* 1986). However, this is not an issue in (1.2) since the source is unique.

Following from these conclusions, understanding the screech mechanism, and the associated mode switching, requires first localising the acoustic source, and investigating the screech loop considering the proper convective velocity. With this purpose, Panda (1999) carried out a near-field mapping of the pressure fluctuations in phase with the screech phenomenon. He found the sound to be emitted somewhere in between the third and the fourth shock tip for mode A2. From successive spark schlieren photographs, Umeda & Ishii (2001) found the dominant source at the rear edge of the third shock cell. Gao & Li (2010) took advantage of numerical simulations to recognise the first five shocks as effective sources for A1, A2, B and C modes, but the dominant source was found between the second and the fourth shock cells. Edgington-Mitchell *et al.* (2014) investigated the C mode, and suggested that acoustic waves are more likely to be emitted somewhere in between the second and the fourth shock cells wherein the coherent vorticity undergoes the largest fluctuations. Raman (1997) also experimentally localised the sound source by using two microphones for a phase evolution survey of screech acoustic waves emitted from a rectangular jet. He figured out that the third shock is responsible for sound radiation at $M_j = 1.45$ and the fourth is involved at $M_j = 1.75$. The results on the localisation of the screech source from the mentioned studies are summarised in table 1.

The aim of the present study is to localise in a systematic fashion the unique source of screech feedback with respect to different modes, and at various setting points within the range of a given mode. The knowledge of the source position permits the estimation of the time spent for an instability to be convected from the nozzle to the source, and for the feedback to reach back to the nozzle. From this, the convective velocity and the period of a screech loop are determined. This experimental investigation is based on measurements of near-field acoustic and schlieren visualisations at high frame rate that provide complementary insights into the features of the acoustic and hydrodynamic phenomena related to screech. In § 2, the experimental set-up is described; then schlieren records are exploited to characterise the screech-associated phenomena near the shear layer in § 3.

M_j	NPR	f_s (Hz)	St_s	Mode	U_j (m s^{-1})	Re_j
1.07	2.06	6508	0.74	A1	335	1.16×10^6
1.10	2.14	5882	0.65	A1	342	1.21×10^6
1.13	2.22	5397	0.59	A1	350	1.26×10^6
1.15	2.27	6024	0.64	A2	355	1.29×10^6
1.23	2.52	3761	0.38	B	374	1.44×10^6
1.32	2.84	3295	0.32	B	394	1.61×10^6
1.35	2.97	3270	0.31	B	401	1.68×10^6
1.37	3.05	3114	0.30	B	406	1.72×10^6
1.45	3.42	2827	0.25	B	422	1.90×10^6
1.50	3.67	2712	0.24	B	432	2.02×10^6

TABLE 2. Setting points of the present study where $St_s = f_s D/U_j$ and $Re_j = \rho_j U_j D/\mu$. NPR and f_s are measured; U_j is calculated.

The localisation of the screech acoustic source is presented in §4, which leads to a description of the screech loop structure for each mode considered in §5. Concluding remarks are finally provided.

2. Experimental set-up

2.1. *Facility*

The studied jets exhaust from a convergent nozzle into the 10 m $\times$ 8 m $\times$ 8 m anechoic room of the Laboratoire de Mécanique des Fluides et d'Acoustique at École Centrale de Lyon. Compressed dry air is supplied by a centrifugal compressor, which allows continuous operation at a maximum flow rate up to 0.85 kg s^{-1}. The maximum nozzle pressure ratio (NPR) is 3.9, corresponding to $M_j = 1.54$. The nozzle diameter is $D = 38$ mm, its nozzle lip is 0.5 mm thick and the contraction ratio is 4.4 : 1 (André 2011). Static pressure is measured in the inlet duct 15 diameters upstream of the nozzle, and is combined with ambient pressure measurements and isotropic flow relations to evaluate M_j. These flow conditions are monitored to ensure that, once set, M_j remains constant within $\pm 0.2\%$. The total temperature is monitored by a K-type thermocouple protruding into the inlet pipe. After a run-time of half an hour, the air supply system is such that the total temperature stabilises at 30 °C $\pm$ 2 °C depending on day-to-day variation of air temperature at the compressor inlet. The ambient temperature in the anechoic room is also monitored by a thermocouple probe located in a region at rest. Results obtained with two different experimental techniques are reported here: high-speed schlieren visualisations of the jet shear layer and its surroundings, and near-field acoustic measurements. These techniques are applied to 10 jets whose corresponding Mach numbers and characteristics are provided in table 2. The screech Strouhal number St_s and the jet Reynolds number Re_j are based on the equivalent fully expanded jet velocity U_j and density ρ_j. Those setting points are chosen to cover the axisymmetric modes A1 and A2, as well as the flapping mode B. Three setting points relate to the A1 mode. Only one deals with the A2 mode because it tends to coexist with another mode as soon as it moves apart from $M_j = 1.15$. Above $M_j = 1.23$, a flapping mode is obtained and is studied through six different setting points, which allows one to assess a potential effect of M_j on the screech loop characteristics for this given mode. These modes are illustrated in appendix A, on the basis of schlieren visualisations.
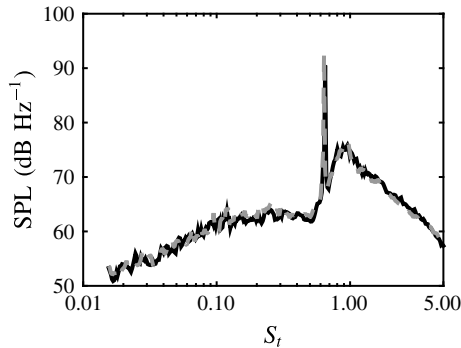
FIGURE 1. Acoustic spectrum for the $M_j = 1.15$ jet measured at a distance of $55D$ from the nozzle, with an angle of $130°$ from the jet axis, in 2011 (——) and 2016 (– – –).

2.2. *Apparatus*

The near-field acoustic measurements are performed using two 1/8-inch B&K 4138 microphones, with a Nexus 2692 conditioner. The first reference microphone is mounted fixed to the nozzle rig; the second is mounted on a motorised rig allowing for axial and radial traverses. The same rig is also used to support the conventional Z-type schlieren system set-up built up from two 200 mm f/8 parabolic mirrors spaced by 2.5 m. The light source is a focused high-power Cree XP-L light-emitting diode (LED). Comparative tests on data post-processing specific to this study led to the knife edge being set perpendicular to the jet axis. Axial density gradients are thus observed. The knife edge cut-off is set to approximately 50 %. Grey-scale images are recorded by a Phantom V12 CMOS camera; the grey-level field is denoted by $g(y, z, t)$. The collecting optics is a Sigma 120–400 mm f/4.5–5.6.

The schlieren films recorded as part of this study arise from two test campaigns. Cases at $M_j = 1.10$ and $M_j = 1.35$ were acquired in 2011 by André, Castelain & Bailly (2011*a*); other cases were acquired in 2016 with identical experimental set-ups. The $M_j = 1.15$ jet is available from the 2011 and 2016 campaigns, so it can be used for checking consistency. Far-field noise spectra measured in 2011 and 2016 at 130° with respect to the jet axis are compared in figure 1. The screech frequency and amplitude are found to be in good agreement in the two campaigns. The peak frequency and the sound pressure level of the broadband shock-associated noise also compare very well with each other. The similarity of the hydrodynamic structure of the $M_j = 1.15$ jets measured in 2011 and in 2016 can also be verified in figure 2 through the juxtaposition of the time-averaged schlieren images. They are also compared in figure 3 by superimposing the profiles along the jet axis of time-averaged grey levels $\bar{g}$. In these two figures, the grey levels are normalised to get around the different light and camera settings. The distance between the leading edge of the second shock cell and the leading edge of the seventh is found to be 1.3 % longer in 2016 than in 2011. This difference may be attributed to the uncertainties emerging from the calibration of the scaling factor, the precision of the setting points, and possible small modifications of the rig undergone between the two campaigns.

2.3. *Schlieren measurement procedure*

Five parameters are taken into account for acquiring the schlieren visualisations. The first one is the spatial extent of the field of view. The second one is the
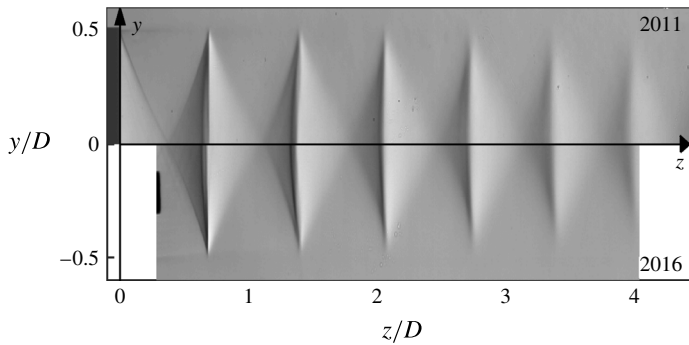
FIGURE 2. Time-averaged grey-level field $\bar{g}(y, z)$ of schlieren images of a $M_j = 1.15$ jet captured in 2011 (top) and in 2016 (bottom).
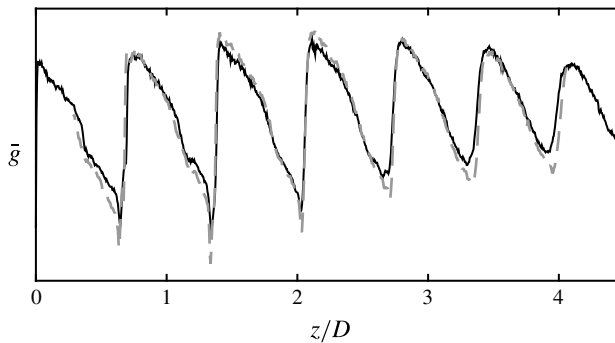

FIGURE 3. Normalised profile of $\bar{g}(z)$ (arbitrary units) on the jet axis computed from schlieren images of a $M_j = 1.15$ jet, in 2011 (——) and 2016 (– – –).

desired sampling rate. These two parameters determine the maximum frame size and the corresponding magnification factor. Finally the exposure time is set by the sampling period and the light intensity. The use of the schlieren visualisation is twofold: to study the turbulent flow in the shear layer and the screech-associated phenomena in the region surrounding the jet. Therefore, two sets of records are available from each campaign. The corresponding camera settings are provided in table 3. One puts priority on the extent of the field of view, and the other prioritises the sampling rate. The minimum acquisition frequency for analysing some flow properties was determined after the work of Veltin, Day & McLaughlin (2011), who found satisfactory results by sampling at 15 times the jet characteristic frequency $f_c = U_j/D_j$, with U_j and D_j the exit velocity and diameter of the equivalent fully expanded jet. For the worst case, $M_j = 1.50$, f_c is approximately 10 kHz, so the sampling rate is chosen higher than 150 kHz. This frequency is reached by reducing the size of the frames in the radial direction while keeping a large axial size. Previous studies summarised in table 1 recognised the source of screech to be located between the second and the fifth shock tips. Consequently, the frame used for this study is chosen to contain at least the first five shock cells. However, this measurement is not achievable on one single frame when M_j is higher than 1.23 because the spatial extent is limited by the mirror diameter. For these cases, the camera is shifted by an increment of 100 mm ($2.6D$) until the fifth shock cell is filmed. The dataset is thus

	Rate (fps)	Exposure (μs)	Size (pixel)	Length (z/D)	Radial limit (y/D)
2011 Shear layer	430 769	2.8	640 × 16	4.2	[0.44; 0.55]
2011 Surroundings	7 200	4.0	1280 × 656	5.2	[−1.48; 1.59]
2016 Shear layer	220 472	4.0	1024 × 24	4.9	[0.44; 0.55]
2016 Surroundings	18 000	2.0	704 × 424	3.8	[−0.61; 1.67]

TABLE 3. Setting of the camera and the lens for the different datasets: fps = frames per second.

composed of several films. Schlieren images must be interpreted with some caution because they are altered by integration effects along the optical path. These artefacts are, however, weaker when the flow is characterised by a strong azimuthal and radial coherence, as with screech.

3. Schlieren visualisations analysis

3.1. *Overview*

A snapshot and time-averaged picture of the schlieren visualisation of the $M_j = 1.15$ jet are presented in figure 4(*a,b*). These images clearly show the quasi-periodic pattern of shock cells consisting of compression and expansion waves. The mean spatial period of this pattern is called the shock cell length L_{sc}. The average image shows the decrease of the shock cell intensity with increasing downstream distance from the nozzle. For each pixel, a time signal $g(y, z, t)$ of grey levels acquired at a high sampling rate is available, and the amplitude of its Fourier transform at the screech frequency, denoted by $G_s(y, z)$, is reported in figure 4(*c*). High values of this coefficient correspond to the darkest regions, and are obtained next to the shock themselves. This high level of fluctuation is attributed to shock oscillation at the screech frequency (Panda 1998; André, Castelain & Bailly 2011*b*). Another remark concerns the presence of lobes in the near field that can be linked to the standing-wave pattern observed by Westley & Woolley (1969). They interpreted this phenomenon as the resultant effect of the interaction between the instability wave convected with the flow and the screech acoustic waves. More details about the lobed pattern can be observed in figure 5, which represents the axial profiles of grey-level fluctuations at the screech frequency. These profiles are measured at a radial position chosen to display the maximum of instability wave features, and therefore as close as possible to the lip line. However, if the measure is conducted too close to the jet, shocks periodically cross the probed line and sharp discontinuities appear in the profile; therefore the interpretation of those results becomes complicated. A convenient position for the measurement line is found along the line at $y/D = 0.55$ for M_j lower than 1.32, and along the line at $y/D = 0.75$ for higher M_j. A look into these profiles shows similarities between all cases. The first observation concerns the lobed shape of the curves, which is similar to the observation in figure 4(*c*) for the $M_j = 1.15$ jet. Considering only the midline of the profiles by putting aside the undulations, a second similarity comes out. The wavy pattern is supported by a bell-shaped curve that points out the amplification rate of instability waves. They first grow with increasing distance from the nozzle, then saturate, and finally decay further downstream.

The wavenumber k_{sw} of the lobed pattern was derived by Panda (1999) from the acoustic and hydrodynamic wavenumbers k_s and k_h, by considering upstream-propagating acoustic and downstream-propagating instability waves. This corresponds
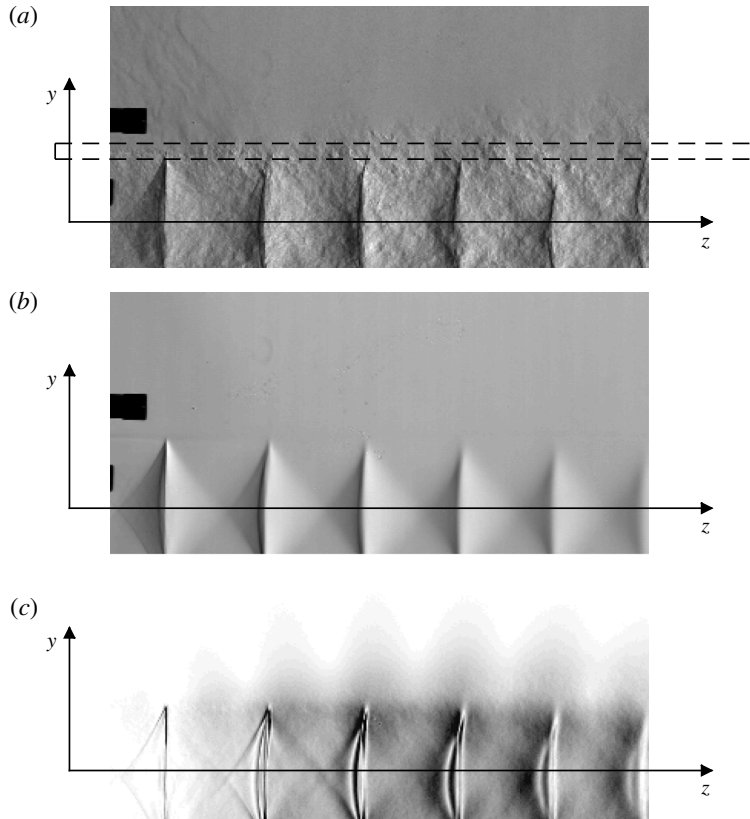
FIGURE 4. (*a*) Instantaneous schlieren image $g(y, z, t)$ (4 µs time exposure). The dashed rectangle shows the field of view of the high-speed records. (*b*) Averaged field $\overline{g}(y, z)$. (*c*) Fluctuating field $G_s(y, z)$ at the fundamental screech frequency from schlieren measurement of a jet at $M_j = 1.15$, mode A2.

to the region upstream of the screech acoustic source, but both waves travel in the same direction downstream of the source. Here we choose to denote by k_{sw}^- the wavenumber of the wave pattern where acoustic is retrograde, and k_{sw}^+ where acoustic is propagative, giving

$$k_{sw}^- = k_h + k_s, \tag{3.1a}$$
$$k_{sw}^+ = k_h - k_s. \tag{3.1b}$$

By convention, all wavenumbers are chosen positive. The corresponding wavelengths $L_{sw}^- = 2\pi/k_{sw}^-$ and $L_{sw}^+ = 2\pi/k_{sw}^+$ can be expressed as a function of the screech frequency f_s, the convective velocity at screech frequency U_c and the speed of sound c_0 in the jet surrounding:

$$L_{sw}^- = \frac{U_c}{f_s(1 + U_c/c_0)}, \tag{3.2a}$$
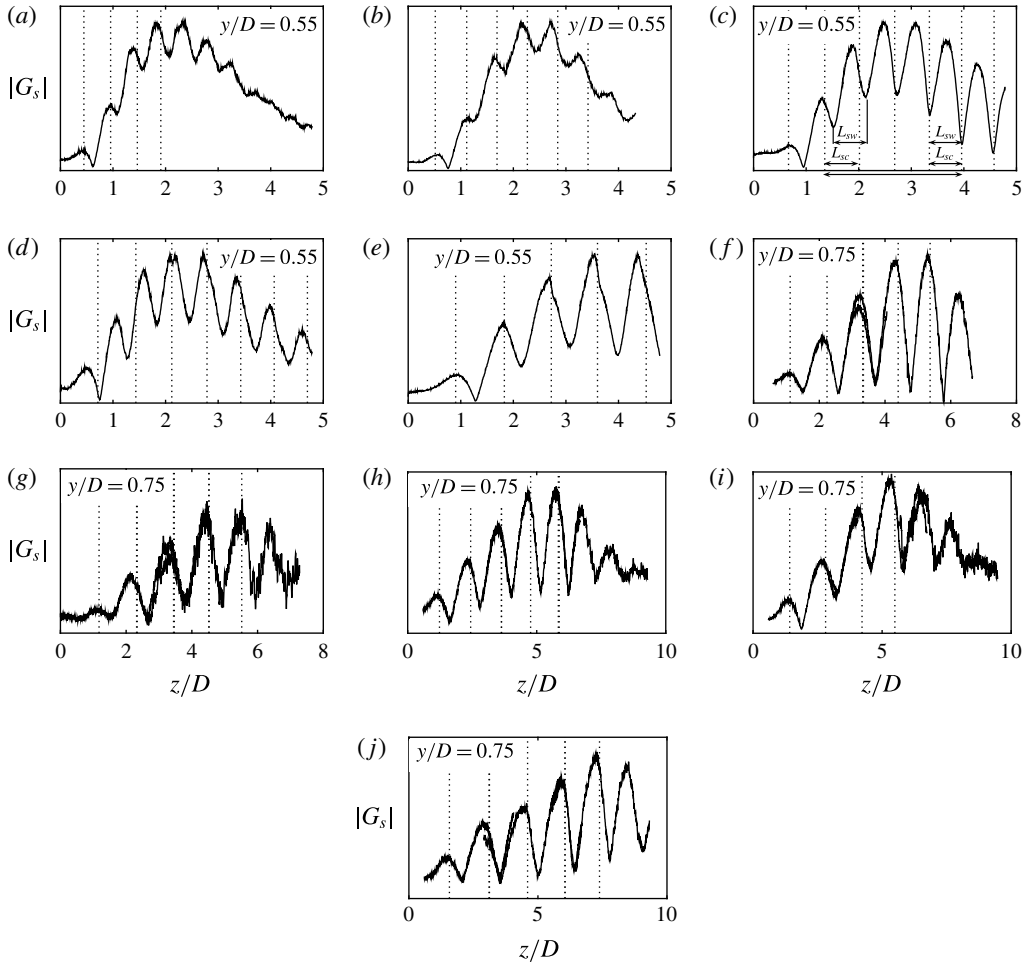$$L_{sw}^+ = \frac{U_c}{f_s(1 - U_c/c_0)}. \tag{3.2b}$$

FIGURE 5. Modulation of the grey-level field G_s at the screech frequency (arbitrary scale) along a line at $y/D = 0.55$: (a) $M_j = 1.07$, (b) $M_j = 1.10$, (c) $M_j = 1.13$, (d) $M_j = 1.15$, (e) $M_j = 1.23$, (f) $M_j = 1.32$, (g) $M_j = 1.35$, (h) $M_j = 1.37$, (i) $M_j = 1.45$ and (j) $M_j = 1.50$. Shock locations are indicated by vertical dotted lines.

As an illustration, if the convective velocity is approximated to $0.6U_j$, these relations provide $L_{sw}^- = 0.63D$ and $L_{sw}^+ = 2.68D$ for the case $M_j = 1.13$, and $L_{sw}^- = 1.20D$ and $L_{sw}^+ = 7.26D$ for the case $M_j = 1.37$.

The profile of $G_s(z)$ for the $M_j = 1.13$ case shown in figure 5(c) covers the first seven shock cells of the jet. Since the source is expected to be located between the second and the fifth shock tips, the source is somewhere within the profile. The lobes, however, are spaced by a distance similar to L_{sw}^-, and there is no clear experimental evidence of a L_{sw}^+ length scale. More generally, the transition from L_{sw}^- to L_{sw}^+ is not visible for all 10 cases, and the observed wavelength is closer to L_{sw}^- than to L_{sw}^+.

Nonetheless, the $M_j = 1.13$ jet presents a notable characteristic that delimits two regions. Upstream of the fourth shock, the lobed pattern wavelength is smaller than the shock cell length, whereas both length scales are equal downstream. The $M_j = 1.15$ jet exhibits the same features: upstream of a region in between the third and the fourth

shocks, the lobes are spaced by a length L_{sw}^- smaller than L_{sc}, and these lengths are equal downstream. These jets are the only two having L_{sw}^- different from L_{sc}. All other cases present only a single wavelength, which appears to be equal to the shock cell length everywhere. Moreover, the similarity between L_{sw}^- and L_{sc} is consistent with Tam's theoretical conclusions about these length scales. According to Tam *et al.* (1986, 2014), a necessary condition for the screech feedback mechanism to be self-sustained is

$$k_h - k_{sc} = -k_s. \qquad (3.3)$$

By comparison with (3.1*a*), $k_h - k_{sw}^- = -k_s$, Tam's theory straightforwardly imposes that $L_{sw}^- = L_{sc}$. This statement is not supported by the present experimental results for both $M_j = 1.13$ and $M_j = 1.15$ cases. However, the difference between L_{sw}^- and L_{sc} is small, although it is clearly observable, which indicates that the condition (3.3) is overly rigid, and the screech conforms with a slightly different condition provided by (3.1*a*). The behaviour of the modulation upstream of the source can thus be explained by the theoretical model relying on the wave superposition.

Downstream of the source, the lobes are not spaced by the distance expected from (3.1*b*). The period of the pattern seems to be equal to the shock cell length. This feature is likely to result from the modulation of the instability wave by the shock cells, and from the weak amplitude of acoustic waves because of the upstream directivity of screech. The role of shock cells in the existence of the lobed pattern can be demonstrated by considering the jets at $M_j = 1.07$, 1.37 and 1.45. For these three Mach numbers, the field of view of the schlieren visualisation is large enough to cover the mixing layer farther downstream from the last detectable shock tip. In each case, the amplitude of lobes starts decaying downstream of the last noticeable shock cell. In addition, the ability of shock cells to modulate the turbulence has been pointed out by André (2012, in his figure 5.33) throughout particle image velocimetry (PIV) measurements in underexpanded screeching or non-screeching jets. Moreover, the absence of the wavelength L_{sw}^+ involved in the acoustic–hydrodynamic interaction downstream of the source can be explained by two reasons. Firstly, k_h and k_s are expected to be close, in particular for the jets at highest Mach numbers, so $k_{sw}^+ = k_h - k_s$ is small and may not be noticeable in the spatial extent of the images. Secondly, far-field measurement at the fundamental screech frequency shows a strong upstream directivity (Norum 1983; Berland *et al.* 2007); thus, even in the near field, screech acoustic waves are likely to be weaker downstream of the source.

Finally, the features of the overall profile can be explained as follows. All along the jet, the instability wave is modulated by the shock cell pattern. This phenomenon could explain by itself the presence of lobes spaced by L_{sc} in the near-field map of screech-associated fluctuations, but jets at $M_j = 1.13$ and $M_j = 1.15$ are characterised by a modulation wavelength L_{sw}^- different from L_{sc} in the first three or four shock cells. This remark suggests that acoustics also plays a role in explaining the lobes where its contribution is strong, but since L_{sw}^- is expected to be close to L_{sc}, the difference between them is not perceptible for all other jets. However, downstream of the source, the acoustic contribution is too weak in comparison to the instability wave, preventing any observation of L_{sw}^+. If L_{sc} coincides with L_{sw}^- in the region upstream of the source, then from (3.1) and (3.3),

$$k_h - k_{sc} = k_h - k_{sw}^- = -k_s = -\frac{\omega_s}{c_0}. \qquad (3.4)$$

This identity will be tested from the analysis of the screech-associated wavenumbers in the next section.

3.2. *Wavenumber–frequency spectrum analysis*

An attempt is made to experimentally determine the different wavenumbers involved in the screech feedback loop. This is carried out through a one-dimensional spatial Fourier transform applied to Fourier coefficients $G_s(z)$ at the screech frequency along the axial direction at $y/D = 0.55$, themselves computed from the high-speed schlieren films. A first analysis is performed in a region located upstream from the source, namely $0 \leqslant z \leqslant z_N$, where z_N denotes the coordinate of the source location. The determination of this position is detailed in the next section, which benefits from the general overview given in the present section. The source is found either at the third or at the fourth shock tip. As a consequence, the discrete Fourier transform is performed over a short extent that contains only two to four wavelengths depending on the case, so the resolution is low in the wavenumber space. The spatial signal $G_s(z)$ used as input to the spatial Fourier transform is weighted by a Gaussian function of width five standard deviations. The wavenumber resolution is improved by doubling the length of the signal by adding zeros. This process is undertaken in order to better distinguish between lobes and randomness, but tests have been performed to ensure that zero padding has no effect on the characterisation of the two main peaks described hereafter.

The result is shown in figure 6 as a solid line. It consists of a pair of dominant peaks, one characterised by a positive wavenumber and a second characterised by a negative wavenumber. The locations of local maxima are estimated using a method from Gasior & Gonzalez (2004) to improve the wavenumber resolution. This method takes advantage of the Gaussian shape of the spectrum calculated from a single-frequency signal windowed by a Gaussian function. The method can be extended to a signal containing more frequencies if their respective Fourier transforms do not overlap. As a consequence, the location of the maximum of a peak can be estimated from the Gaussian function that best fits the peak. The three points on the top of the peaks are used for fitting in this study. Gasior & Gonzalez (2004) reported a maximum error of less than 1 % of the frequency resolution. In the present study the worst resolution is found to be 80 rad m^{-1} for the $M_j = 1.07$ jet without zero padding. An error of less than 1 % would lead to an error of less than 0.8 rad m^{-1}. In order to assess the method, the spatial spectra along all the available radial positions have been computed. The results are found to be weakly dependent on the considered radial position, except for $M_j = 1.45$, probably because the distance between the peaks in the wavenumber space is small. In addition, this case exhibits strong shock oscillations that intercept the probed line, causing large discontinuities that produce a significant amount of harmonics. These are likely to influence the determination of the maximum of peaks. The same problem is observed for the $M_j = 1.50$ jet. In general, the error observed from the lowest peaks is found to be larger, because the effect of overlapping is more significant.

The maxima of the peaks are marked by crosses in figure 6, and are tabulated in table 4. The wavenumber corresponding to the retrograde screech acoustic wave $-k_s = -\omega_s/c_0$ is represented by a dotted line. The comparison between this prediction and the maximum of the peak in the negative wavenumber range shows a good agreement, as also reported in table 4. It provides some confidence to state that this peak is related to the upstream-propagating acoustic wave. As for the peak in positive wavenumbers, it is expected to be $k_h = \omega_s/U_c$; the corresponding convective velocity is provided in table 4 normalised by U_j, and is indeed roughly equal to $0.6U_j$ for all cases. This result is consistent with many studies, for instance those by Powell *et al.* (1992), Massey & Ahuja (1997) or Panda & Raman (1997).
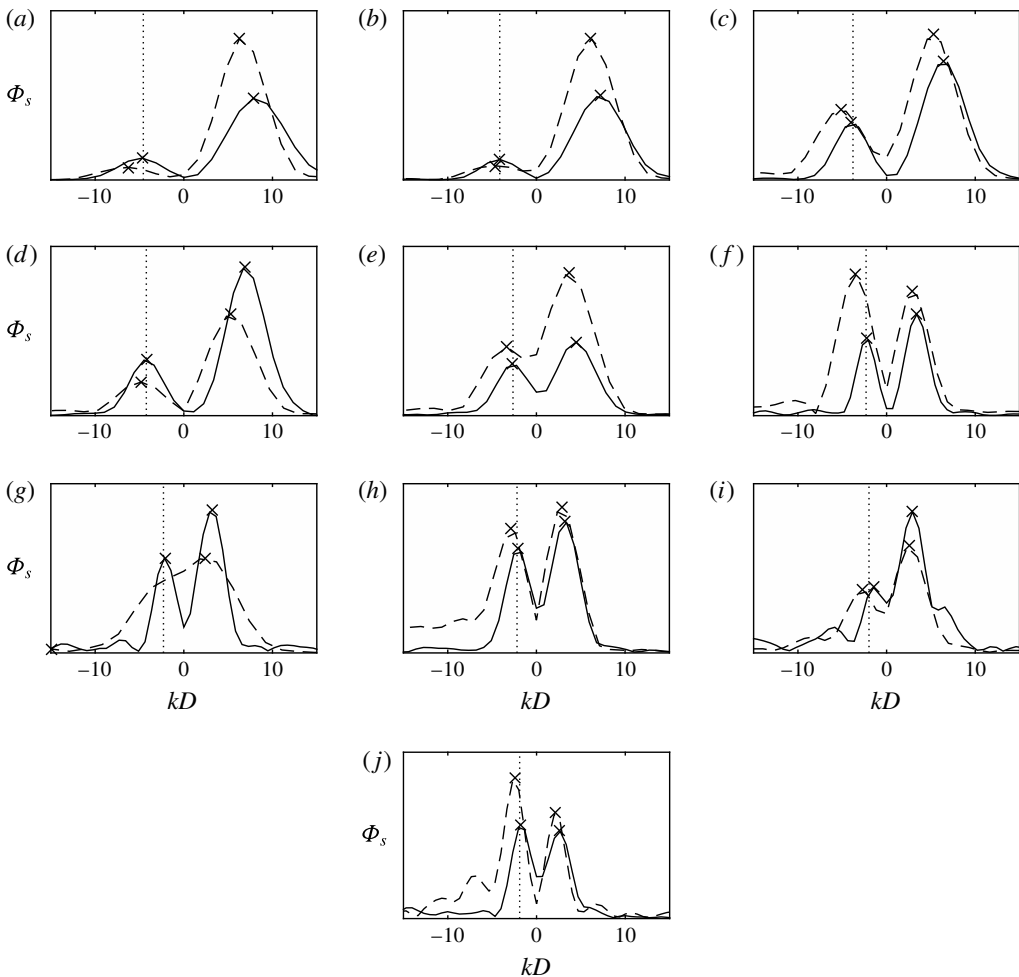
FIGURE 6. Wavenumber spectrum at screech frequency Φ_s (arbitrary linear scale) upstream of the source (——) and downstream (– – –): (*a*) $M_j = 1.07$, (*b*) $M_j = 1.10$, (*c*) $M_j = 1.13$, (*d*) $M_j = 1.15$, (*e*) $M_j = 1.23$, (*f*) $M_j = 1.32$, (*g*) $M_j = 1.35$, (*h*) $M_j = 1.37$, (*i*) $M_j = 1.45$ and (*j*) $M_j = 1.50$. The wavenumber $k_s = -\omega_s/c_0$ is indicated by the vertical dotted line.

The speed of sound tabulated in table 4 is not equal to the speed of sound of 337 m s^{-1} expected from the ambient temperature measured during the experiment. An error of 5 % or less is observed for seven of the 10 cases. A larger error is noticed for the $M_j = 1.35$, 1.45 and 1.50 jets, in particular for $M_j = 1.45$, whose validity has already been examined and called into question. Unfortunately, that dispersion prevents us from providing evidence for the existence or absence of an eventual other type of feedback mentioned by Shen & Tam (2002), Chatterjee, Ghodake & Singh (2009) or Edgington-Mitchell, Honnery & Soria (2015).

Finally, the last column of table 4 compares the wavenumber $k_{sw}^- = k_h + k_s$ associated with the lobed pattern, see (3.1*a*), to the shock cell wavenumber averaged over $0 \leqslant z \leqslant z_N$. The shock positions are measured from the centreline grey profiles of the averaged schlieren images with an accuracy of $\pm 0.007D$ arising from the width of the shocks, and an additional error of $\pm 0.04z$ from the scaling factor of pixels, but these

M_j	Range (z/D)	$-k_s$	k_h	$c_0 = \omega_s/k_s$	$U_c/U_j = \omega_s/(k_h U_j)$	$(k_h + k_s)/k_{sc}$
1.07	[0, 2.0]	−128	215	319	0.57	1.03
1.10	[0, 2.3]	−111	188	334	0.57	1.03
1.13	[0, 2.7]	−103	169	328	0.57	1.10
1.15	[0, 2.8]	−111	184	340	0.58	1.28
1.23	[0, 2.8]*	−70	116	337	0.54	1.05
1.32	[0, 4.6]	−60	89	347	0.59	1.04
1.35	[0, 4.3]**	−56	83	367	0.61	1.01
1.37	[0, 3.7]*	−55	85	355	0.57	1.04
1.45	[0, 4.3]*	−36	77	493	0.55	0.97
1.50	[0, 4.7]*	−45	67	379	0.59	1.05

M_j	Range (z/D)	$-k_d^-$	k_h	$U_c/U_j = \omega_s/(k_h U_j)$	$(k_h + k_d^-)/k_{sc}$
1.07	[2.0, 4.0]	−168	174	0.70	—
1.10	[2.3, 4.3]	−122	161	0.67	0.99
1.13	[2.7, 4.7]	−136	139	0.70	1.05
1.15	[2.8, 4.7]	−128	141	0.75	1.04
1.23	[2.8, 4.7]*	−87	99	0.64	1.02
1.32	[4.6, 7.3]	−93	78	0.67	1.07
1.35	[4.3, 6.3]	—	—	—	—
1.37	[3.7, 7.3]*	−77	73	0.66	1.08
1.45	[4.3, 7.3]*	−73	69	0.61	1.16
1.50	[4.6, 9.3]*	−65	53	0.74	0.96

TABLE 4. Wavenumbers of peaks in amplitude of the spatial Fourier transform applied along a line at $y/D = 0.54$ over the given axial range on high-speed schlieren records that correspond to the region from the nozzle to the fourth shock tip, except for cases marked by *, which denotes the third shock tip. In the case marked **, the extent was limited by the field of view of the record. The shock cell wavenumber is determined from shock cells contained within the range given in the second column.

uncertainties are insignificant in comparison to the margin of error pointed out on k_s. The modulation wavenumber is found to be larger than the shock cell wavenumber by a few per cent, except for the case $M_j = 1.15$ that exhibits k_{sw} 28 % larger than k_{sc} because of the jump in frequency, whereas no change in aerodynamic characteristics of the jet is observed (Clem, Zaman & Fagan 2016). The second largest k_{sw}^- in comparison to k_{sc} is found for case $M_j = 1.13$: k_{sw}^- is 10 % larger than k_{sc}. The case $M_j = 1.45$ should not be considered because of the problem of peak overlapping mentioned above. These results are consistent with the conclusions of § 3.1: $k_h - k_s$ is actually close to k_{sc}, so L_{sw}^- is close to L_{sc}, for all but the $M_j = 1.13$ and $M_j = 1.15$ cases.

A procedure similar to the one outlined for the region upstream of the source is applied for $z_N \leqslant z \leqslant z_{max}$, where z_{max} is the maximum reachable distance with respect to the schlieren record. The results are plotted as a dashed line in figure 6. The peak in positive wavenumbers is still associated with the instability wave. The corresponding convection velocity is summarised in table 4. Its value is found to be close to $0.7 U_j$, hence slightly higher than upstream of the source. A trend of rising convective velocity with axial location was observed by Gojon *et al.* (2015) from a numerical study, and from the same experimental data as the present study but using a different method by Mercier, Castelain & Bailly (2016). Regarding the peak

in negative wavenumbers denoted by k_d^-, the distance between this peak and k_h is compared to k_{sc} in the last column of table 4, with k_{sc} estimated from the shock cells visible in the range of the spatial spectral analysis. Since the shock cell structure fades out with downstream distance, the estimation of k_{sc} can only be approximate by comparison with the accuracy mentioned for the first few shocks. Nonetheless, the comparison highlights the similarity of these two values in most cases. The $M_j = 1.45$ case again shows a surprising result in terms of both k_h and $(k_h + k_d^-)/k_{sc}$ values. In addition to the peak overlapping, the absence of clearly detectable shocks downstream of the fourth one must be pointed out. Thus, comparing $(k_h + k_d^-)$ to k_{sc} might not be relevant. For all other cases, the peak in negative wavenumbers $k_d^- \simeq k_{sc} - k_h$ is recognised as the interaction between the shock cell pattern and the instability wave. The corresponding phase velocity ω_s/k_d^- is subsonic for all cases. No wavenumber peak associated with a retrograde acoustic wave is observed, which is consistent with the determination of the source location z_N. No propagative acoustic wave is detected; this is likely to be attributed to the screech directivity, weaker in the jet axis direction with respect to the upstream direction (Norum 1983; Berland *et al.* 2007).

4. Source localisation through near-field acoustic measurements

Schlieren measurements provide information about screech-associated phenomena in a region where the hydrodynamic contribution is predominant. Regarding the objective of localising the screech source, it is interesting to gain insight into screech-associated fluctuating pressures in the jet near field, where the hydrodynamic pressure field is faded enough so that acoustics becomes the dominant contribution. To this end, two types of near-field measurements are set up. The first is a microphone traverse along a line perpendicular to the jet axis within the nozzle exit plane for Mach numbers 1.13, 1.15 and 1.35 only. The second is a microphone traverse along a line parallel to the jet, and distant by $1.5D$ from the axis (or $2D$ for cases $M_j = 1.45$ and 1.50, to avoid microphone overload). This is repeated for all cases of table 2. For these axial and radial surveys, two microphones are used; one is fixed and constitutes the reference signal, the second is moved by increments of 3–5 mm so as to measure approximately 20–30 points per screech acoustic wavelength. The signals of the two microphones are sampled synchronously at 204 800 Hz for 2 s. The radial traverse is conducted from $y/D = 0.5$ to $y/D = 8$. In the axial direction, the moving microphone travels between $z/D = -0.1$ and $z/D = 6$ for M_j up to 1.23, and down to $z/D = 8$ for higher Mach numbers.

The post-processing of the axial and radial near-field surveys is performed for the same purpose. The phase difference at screech frequency between the moving and the fixed microphones is compared to the expected phase difference if the acoustic source were located at a given position. This method was used by Raman (1997) to determine the source of screech noise in rectangular jets. According to the literature on screech radiation that is summarised in table 1, the screech is likely to be emitted from one predominant source; under this assumption, and if this source can be regarded as a simple monopole, the expected phase lag $\Delta\phi$ between two microphones located at distances r and r_0 from the source is given by

$$\Delta\phi = k_s(r - r_0). \tag{4.1}$$

Two more assumptions are chosen here to constrain the study: the virtual source is located on the lip line in the radial direction, and at a shock tip in the axial direction.

4.1. *Radial traverse*

In the radial configuration, the reference microphone is fixed at $z = -1.8D$ and $y = 1.8D$ considering the centre of the grid as a reference with a precision of $\pm 0.03D$. The mobile microphone moves along the y direction by steps of 3–5 mm from $y = 0.5D$ to $y \simeq 8D$. The position of the rig is accurately measured at each step. Both microphones are in a region upstream of the jet in which screech is strong, and there is no contribution from the hydrodynamic pressure field; the signals are therefore clean and the phase lag variation along the probed line is expected to be smooth. The relative phase is deduced from the cross-spectrum of the two signals at the screech frequency. It is then unwrapped by adding 2π at the corresponding jumps, and finally compared with the predicted phase lags. Results for Mach numbers 1.13, 1.15 and 1.35 are presented in figure 7, through the entire spatial range in figure 7(*a,c,e*), and zoomed in closer to the nozzle in figure 7(*b,d,f*). The predicted phase lag is superimposed onto experimental results for three different source locations: the third, the fourth and the fifth shock tips.

Two regions of different behaviour can be observed in these results. For y/D between 0.5 and 4, the phase follows a pattern in fairly good agreement with the results predicted from (4.1). Farther, for y/D between 4 and 8, the phase draws unexpected patterns, particularly for the jets at $M_j = 1.13$ and 1.35. The choice of the shock corresponding to the screech acoustic source is not straightforward. There is no clear demarcation that would designate unambiguously the source location – the choice might change according to whether the considered region is only y/D between 0.5 and 4, or all the available spatial domain. Nevertheless, the interpretation of the results must be discussed when the distance to the nozzle increases. In fact, the fourth shock is located at $z/D = 2.7$, 2.9 and 4.8 for $M_j = 1.13$, 1.15 and 1.35 respectively. When the moving microphone is at $y/D = 4$, the angle formed between the jet axis and the lines linking the microphone to the source is 124°, 126° and 140°. Norum (1983) investigated the directivity of screech for B and C modes. He observed for the B mode a maximum of screech amplitude at angles close to 170°, and a drop of 10 dB at an angle of 133°, and again a 10 dB drop to reach 123°. These observations were made in the far field, and are therefore not directly applicable in the near field. Nevertheless, measurements of the screech pressure level across the moving microphone path are presented for the case $M_j = 1.35$ in figure 8. They exhibit the same sharp decrease of amplitude with increasing distance from the nozzle as expected from far-field data. The level is decreased by 20 dB at $y = 5.5D$. The lower the amplitude of the screech acoustic wave, the higher the influence of reflection and other contributions to phase measurement. For this reason, the result of this experiment must be considered with caution when y goes up. After these remarks, the results should not be regarded in the entire domain, and a look back at figure 7(*b,d,f*) leads us to conclude that the source is located between the third and the fifth shock tips. A better precision in source localisation cannot be obtained with the present method because the displacement of the source does not induce a sufficient phase shift between the two microphones. Better results would be obtained if one of the two microphone phases was less sensitive to the source location. In this configuration, a displacement of the source would involve a larger variation in phase for one microphone than for the other. This is obtainable by placing the reference in the plane perpendicular to the jet axis that passes through the expected source, so r_0 in (4.1) would be only slightly sensitive to the variation of source location, and $\Delta\phi$ would mostly be dependent upon r. This method requires *a priori* knowledge of the result, but this problem is circumvented by moving a microphone along a line parallel to the jet.
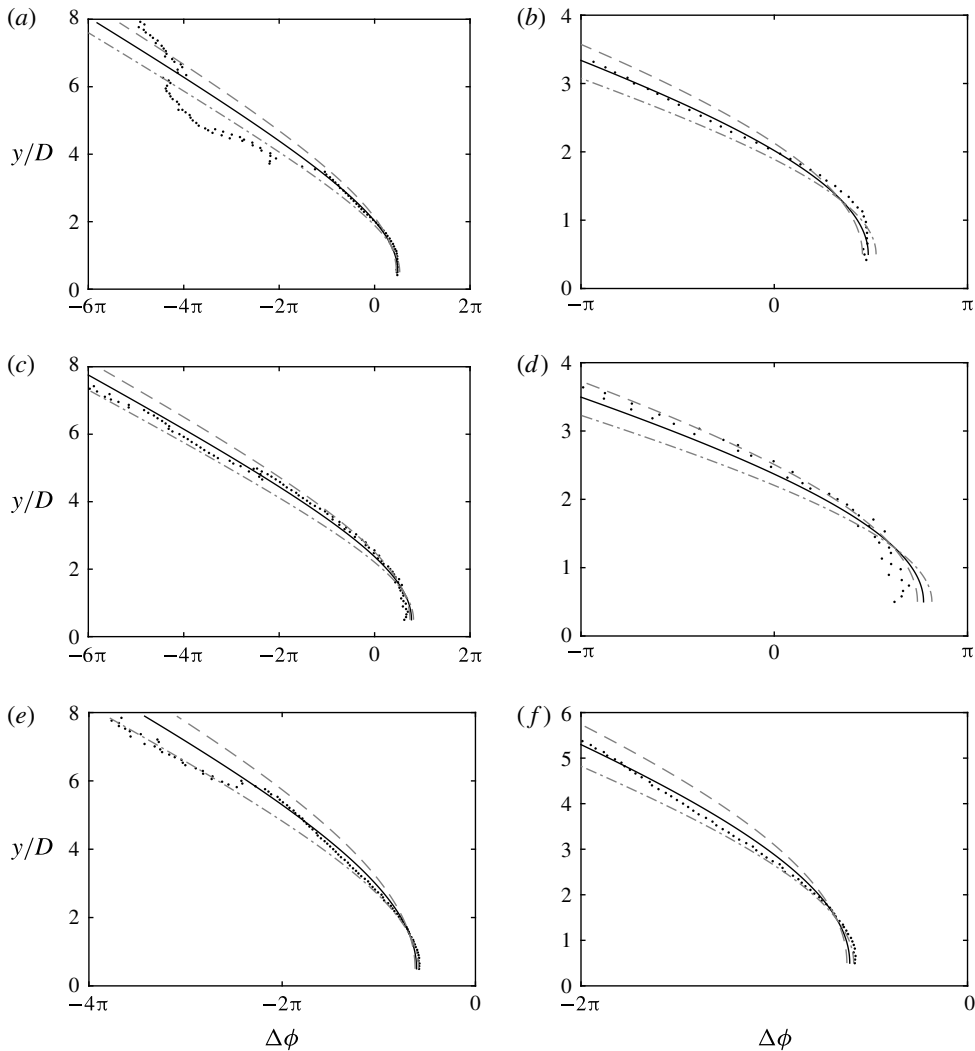
FIGURE 7. Comparison between the experimental and the expected phase lag between a reference microphone and a microphone moving along a line perpendicular to the jet axis in the nozzle exit plane. Graphs on the right are the same as graphs on the left but focused close to the nozzle. Curves: ——, fourth shock tip; — · —, third shock tip; – – –, fifth shock tip; · · · · · ·, measurements. Jet Mach number: (*a,b*) $M_j = 1.13$, (*c,d*) $M_j = 1.15$, (*e,f*) $M_j = 1.35$.

4.2. *Axial traverse post-processing*

In the axial configuration, the reference microphone is fixed at $y = 2.4D$ and $z = 0.4D$ with the same precision of $\pm 0.03D$ as mentioned for the radial traverse. The moving microphone measures the fluctuating pressure along the z direction by steps of 3–5 mm from $z = -0.1D$ to $z = 6D$ or $8D$. In contrast to the radial traverse, in this configuration the microphone is moved along a line close to the jet, and the fluctuating pressure results from the contribution of the acoustic and of the hydrodynamic pressure fields. The interaction between these two waves modulates the
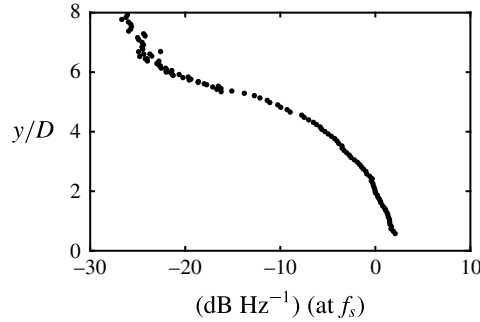
FIGURE 8. Sound pressure level (SPL) measured by the moving microphone SPL normalised by the reference microphone SPL in dB Hz^{-1} at f_s, for $M_j = 1.35$ along the radial traverse in the nozzle exit plane.

amplitude, the phase velocity and the spatial phase evolution of the resultant wave. This modulation makes it difficult to distinguish the 2π phase jumps from regular sharp variations in the region where the hydrodynamic pressure field is strong. This is a source of ambiguity for the unwrapping process; the problem is exacerbated because strong hydrodynamic fluctuations are expected to occur near the screech radiation source. For this reason we chose not to use classical methods for phase analysis such as cross-spectrum or cross-correlation, but to extract the screech coherent signal from random fluctuations by performing a phase average analysis. Such an analysis allows for tracking a single phase-averaged wavefront, and as a consequence avoids the 2π indeterminacy problem.

The phase average is performed for all probed locations along the measurement line. At each location, two synchronous signals are available, one from the reference microphone and the other from the moving microphone. The aim of the first step is to extract the phase at screech frequency provided by the fixed microphone, which will serve as the reference. The signal from the moving microphone will be sorted according to this reference in a second step. To this purpose, the signal measured on the fixed microphone is bandpass-filtered around the screech frequency. The filter is a finite impulse response (FIR) type with cut-off frequency at $\pm 10\%$ of f_s and a drop of 30 dB at $\pm 30\%$ of f_s. This filter is applied with a zero-lag method to ensure that the phase of the filtered signal does not become frequency-dependent, so there is no bias in the case of slight drift of the screech frequency. The resulting clean signal is the phase reference, and its maxima delimit the periods of screech. All periods of the record are then discretised into 20 bins of equal length that correspond to 20 increments of phase in a screech period. The samples of the moving microphone record that are in the same bin with respect to a period, and thus in phase, are averaged. This process is repeated for all longitudinal locations of the experiment. A complementary sketch presenting the method is provided in figure 9. In this figure, the phase axis is displayed between 0 and 4π; the phase average is performed over two consecutive periods because the wavefront tracking requires that the followed wavefront has enough time to travel from the source to the limits of the measured domain, here $z = 0$ and $z = 6$ or $8D$.

Phase-averaged results of all probed locations are in phase with the same reference; the spatial wave can therefore be rebuilt for each phase step. The spatial distribution of the coherent fluctuating pressure p_s against the phase with respect to the screech
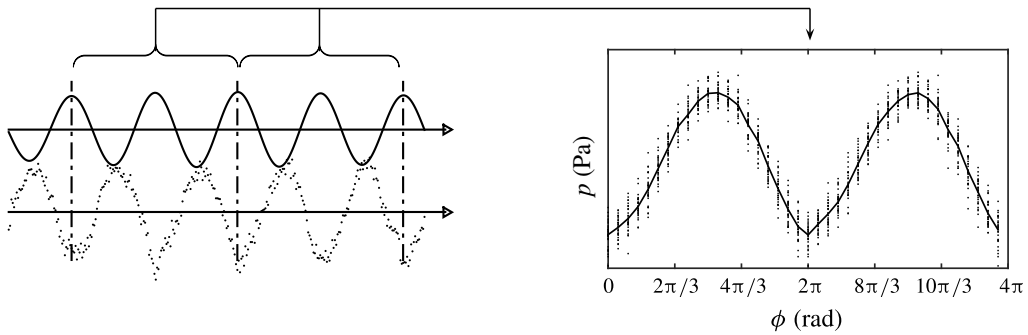
FIGURE 9. Example of phase average process. On the left: ——, reference bandpass filtered signal; ······, moving microphone signal; |, period marks. On the right: ······, data from the moving microphone sorted with respect to their phases; ——, phase-averaged signal.
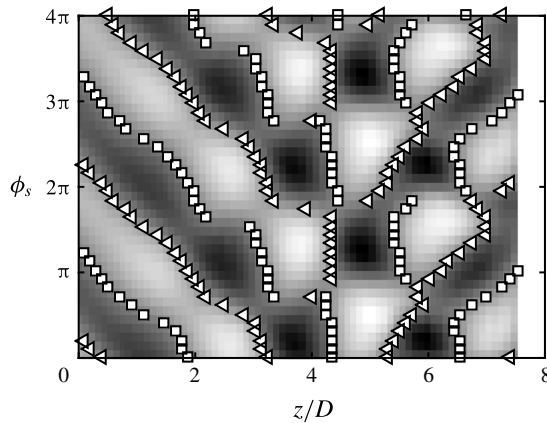

FIGURE 10. Coherent fluctuating pressure along a line at $y = 1.5D$ against the phase with respect to screech cycle in the jet $M_j = 1.32$ near field. The locations of the wavefronts are reported for the 40 phase steps: □, rising edges; ◁, falling edges.

cycle ϕ_s is provided in figure 10 for the $M_j = 1.32$ jet. The zero crossing points of the coherent fluctuating pressures are marked by squares or triangles depending on whether they correspond to a rising or a falling edge. These zero crossing points form a pattern which depicts curved lines representing the wavefronts of screech-associated waves. The direction of propagation of these waves is reversed near $z = 5D$. Considering the rising and the falling edges, four wavefronts can be observed in each direction. Both upstream and downstream of the slope inversion position, one of the wavefronts is found to be continuous from the source to the limits of the domain, and is selected to be compared with the expected phase variation $\Delta\phi$ calculated from (4.1).

4.3. *Experimental results on source location*

The spatial phase evolution of the screech phenomenon is studied across an axially oriented measurement line. This survey aims at investigating the axial evolution of the
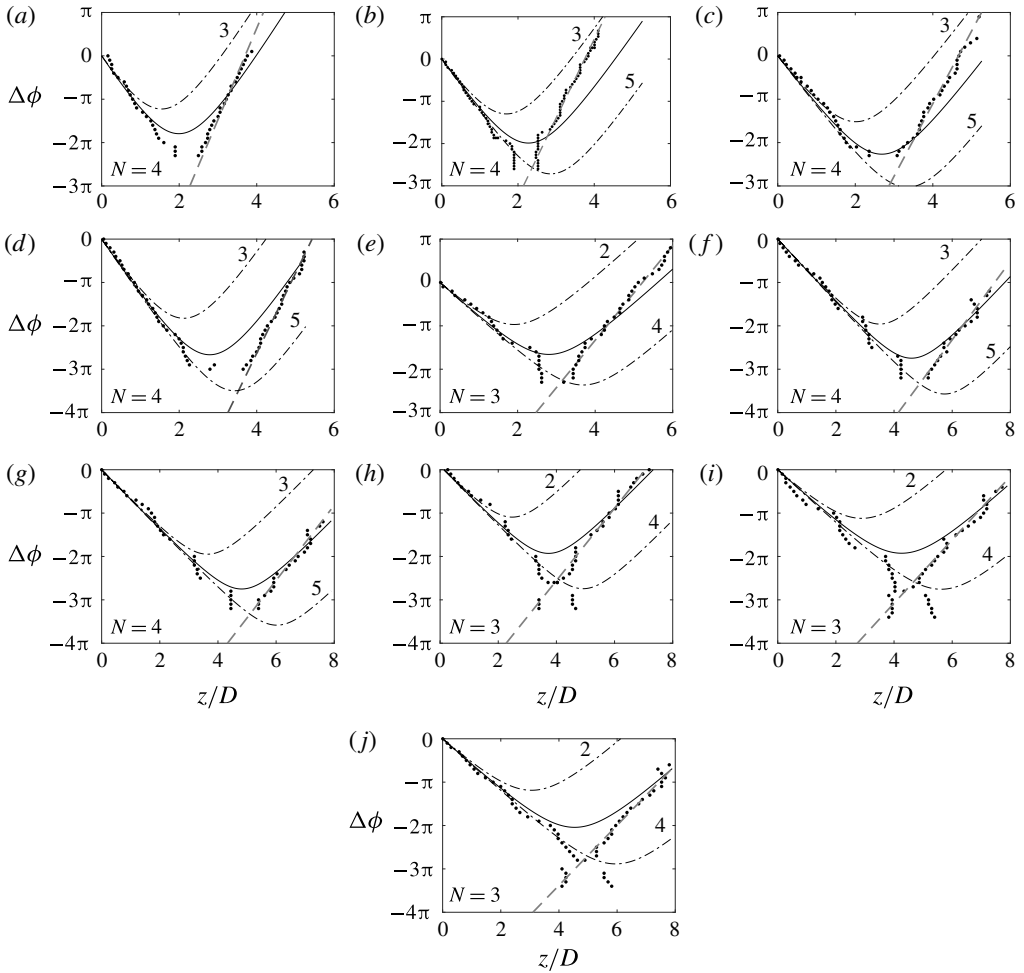
FIGURE 11. Comparison between the experimental and the expected phase lag between a reference microphone and the microphone moving parallel to the jet at (*a–f*) $y = 1.5D$ and (*g–j*) $y = 2D$: $\cdots\cdots$, $\Delta\phi$; $---$ $\mathrm{d}\phi_s/\mathrm{d}z = 2\pi f_s/(0.7U_j)$; ——, the expected result for the source at the shock N; and $-\cdot-$, at the labelled shock. Jet Mach number: (*a*) $M_j = 1.07$, (*b*) $M_j = 1.10$, (*c*) $M_j = 1.13$, (*d*) $M_j = 1.15$, (*e*) $M_j = 1.23$, (*f*) $M_j = 1.32$, (*g*) $M_j = 1.35$, (*h*) $M_j = 1.37$, (*i*) $M_j = 1.45$ and (*j*) $M_j = 1.50$.

phase lag. It concerns all the cases defined in table 2. The experimental results are compared with the corresponding expected phase lag in figure 11. A first look at this figure shows that the experimental results exhibit a slope sign inversion at a certain location as well as the expected phase lag. The slope $\mathrm{d}\phi_s/\mathrm{d}z$ is inversely proportional to the phase velocity of the wave projected onto the line along which the microphone is moved. The inversion of the sign of the slope translates to the inversion of the direction of wave propagation. In the present study, upstream of the location of slope inversion, the wave propagates upstream and conversely downstream. The study of the slopes of the upstream and downstream branches of the phase evolution provides information about their nature.

Considering only the upstream branch, the measured and the expected phase variations are similar. It is then concluded that the wavenumber of the measured phenomenon is the same as used in the model given in (4.1), k_s, for a speed of sound $c_0 = 337$ m s^{-1}. The wave detected in this region corresponds to the screech acoustic wave.

The measurement across the downstream branch diverges from the prediction. This divergence comes from a difference of slope, that is, a different speed of propagation. The slope of the measured axial phase evolution is higher than the predicted slope for an acoustic wave; the phase velocity of the phenomenon is thus lower than the speed of sound. The near-field pressure at the screech frequency is composed of acoustic and hydrodynamic contributions. The hydrodynamic convective velocity is subsonic for all the cases and is therefore eligible for explaining the slope of the downstream branch. This is also consistent with the conclusion of §3 stating the absence of acoustic signature downstream of a given region. The slope of the measured phase evolution is compared to the expected slope considering a convective velocity $U_c = 0.7 U_j$, which corresponds to estimation from the wavenumber analysis in §3. This slope is

$$\frac{\mathrm{d}\phi}{\mathrm{d}z} = \frac{\omega_s}{U_c}. \tag{4.2}$$

The hydrodynamic pressure field is attached to the coherent structures that travel inside the mixing layer almost parallel to the jet axis, and to the line of measurements; thereby, there is no effect of projection. The hydrodynamic phase velocity measured by the microphone traverse is directly equal to the convective velocity. A line of slope corresponding to $U_c = 0.7 U_j$ is added as a grey dashed line in figure 11. This line fits the experimental results well, demonstrating that the downstream-propagating branch is dominated by hydrodynamic near-field pressure. The instability wave at the screech frequency is recognised in §3.1 to be strongly modulated by shock cells, resulting in nodes and antinodes of its amplitude. Thus, the relative acoustic and hydrodynamic amplitudes are dependent upon z. For a given acoustic pressure level, hydrodynamics might dominate at antinodes of the instability wave, and might be dominated by acoustics at nodes. Upstream of the source, the slope of acoustic associated phase lag is negative, and turns positive downstream of the source. The slope of hydrodynamic associated phase lag is positive everywhere. Therefore, wherever the slope is negative, the acoustic pressure field dominates, and the source is necessarily located downstream. This observation sets an upstream limit for the source location, but the downstream limit is still not defined. The source is assumed to be located at a distance of one shock cell or more downstream from the position where the negative slope turns positive. Then, between the inversion location and the source, the positive slope would be sustained by the dominance of the hydrodynamic contribution. Yet, since this contribution is modulated with a wavelength of one shock cell, acoustic should become stronger than hydrodynamic at a certain location upstream of the next shock, so the slope would turn negative again, in contradiction with our first hypothesis. Therefore, the source must be located somewhere in between the last place of negative slope and one shock cell downstream. Constraining the screech source to be located at a shock tip, the shock tip number N corresponding to the source is selected for being the first shock downstream of the last negative slope location. The expected phase lags obtained from the previous and the next shock tips are also included in figure 11 in order to show that there is no ambiguity in finding which agrees better. The fourth shock is found to be the source for all cases except $M_j = 1.23$, 1.37, 1.45 and 1.50. The source is the third shock tip for these four cases.

M_j	Mode	N	m	z_N/D	$\overline{U_c}/U_j$ (from table 4)	$\overline{L_{sc}}/D$
1.07	A1	4	4	2.0	0.53 (0.57)	0.48
1.10	A1	4	4	2.3	0.55 (0.57)	0.57
1.13	A1	4	4	2.7	0.58 (0.57)	0.67
1.15	A2	4	5	2.8	0.56 (0.58)	0.70
1.23	b	3	3	2.7	0.52 (0.54)	0.90
1.32	B	4	4	4.5	0.57 (0.59)	1.13
1.35	B	4	4	4.8	0.59 (0.61)	1.20
1.37	b	3	3	3.8	0.56 (0.57)	1.25
1.45	b	3	3	4.3	0.59 (0.55)	1.43
1.51	—	3	—	4.8	— (0.59)	1.61

TABLE 5. Summary of results about the screech loop structure: n = number of the radiating shock tip; m = number of screech periods per loop; z_N/D = location of the source; $\overline{U_c}/U_j$ = mean convective velocity from the nozzle to the source derived from the phase analysis and, in brackets, from the wavenumber analysis; $\overline{L_{sc}}/D$ = mean shock cell length upstream of the source.

The source locations and the associated shock tips are summarised for all cases in table 5. Since acoustic sources are identified, the screech loop is delimited in space, and can be examined in a suitable domain as discussed in §3.

5. Screech loop

The screech loop is composed of the instability wave convected from the nozzle to the source, and of the acoustic feedback from the source to the nozzle. The travel along this loop takes time T_{loop} given by

$$T_{loop} = \frac{z_N}{\overline{U_c}} + \frac{z_N}{c_0}, \qquad (5.1)$$

with z_N the distance from the nozzle to the shock tip N recognised as the screech source, and $\overline{U_c}$ the mean convective velocity between the nozzle and the source. Assuming that a new structure is triggered exactly when the acoustic wave reaches the nozzle, acoustic and hydrodynamic must be in phase at the nozzle exit. In other words, the total time spent along the loop T_{loop} is necessarily a multiple m of the screech period T_s. In terms of phase, this statement requires the total phase spent along a loop $\phi_{loop} = 2\pi T_{loop}/T_s$ to be a multiple of 2π. The phase of the screech-associated phenomena ϕ_s is calculated along the line $y/D = 0.55$ from high-speed schlieren records. A series of cross-spectra are computed between the grey-level signal of a pixel at the nozzle exit $g(0.55D, 0, t)$ and the signal of another point moving along the z direction $g(0.55D, z, t)$. For each cross-spectrum, the phase at the screech frequency ϕ_s is extracted. The result is then unwrapped to obtain a continuous curve and, if needed, is shifted by increments of 2π to ensure that the prolongation of the positive slope part of the curve downstream approximately crosses $z = 0$ at $\phi_s = 0$. This curve is finally displayed on a (z, ϕ_s) plane in figure 12.

Two characteristics common to all cases, except for $M_j = 1.50$, are noticed in figure 12. The first feature is the inversion of the slope of the curve upstream of the second shock. This observation is related to the local ratio of the amplitude of the hydrodynamic and acoustic waves: close to the nozzle, the hydrodynamic wave
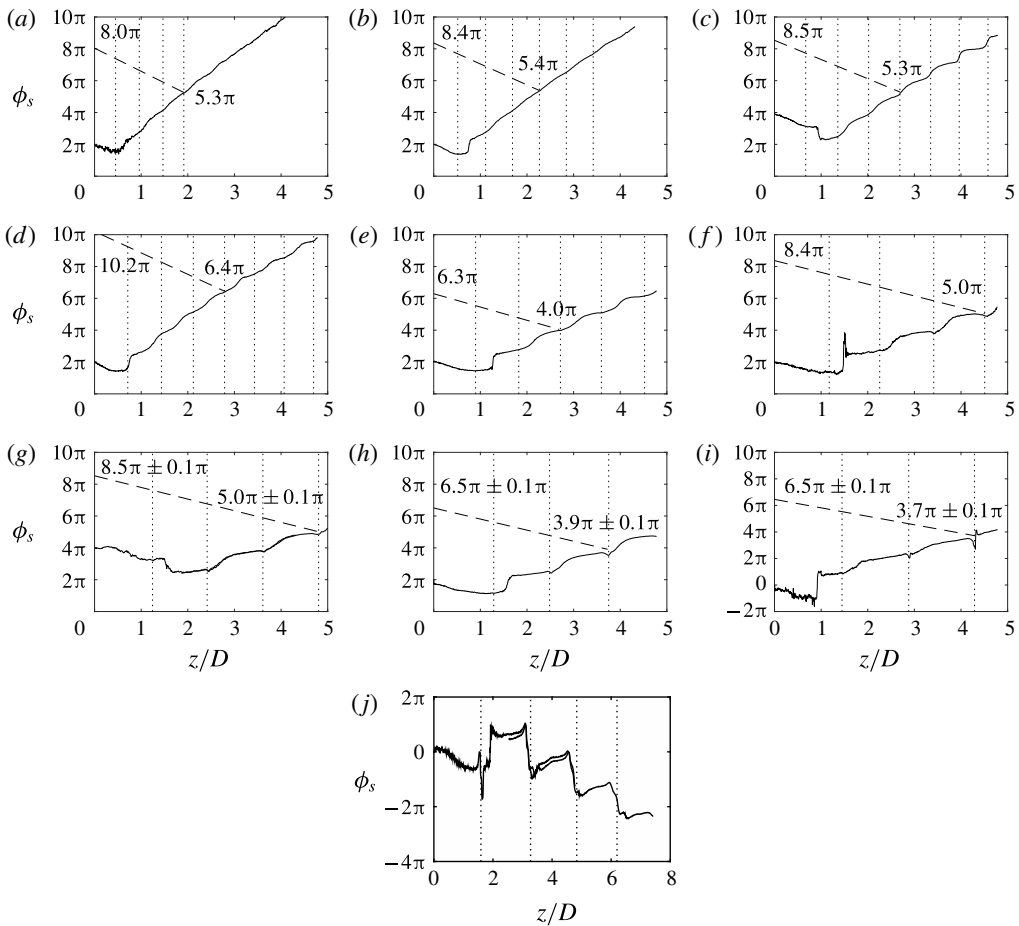
FIGURE 12. Phase evolution $\phi_s = 2\pi t/T_s$ extracted from the cross-spectrum between a pixel at the nozzle and a pixel moving along the line $y/D = 0.55$: $---$, acoustic feedback at 337 m s^{-1}; shock locations are indicated by vertical dotted lines. Jet Mach number: (*a*) $M_j = 1.07$, (*b*) $M_j = 1.10$, (*c*) $M_j = 1.13$, (*d*) $M_j = 1.15$, (*e*) $M_j = 1.23$, (*f*) $M_j = 1.32$, (*g*) $M_j = 1.35$, (*h*) $M_j = 1.37$, (*i*) $M_j = 1.45$ and (*j*) $M_j = 1.50$.

grows, but is weak compared to the acoustic feedback. This is the receptivity region, characterised by a negative slope corresponding to a wave propagating upstream. The case depicting the earliest slope inversion is $M_j = 1.07$; the inversion occurs at $z/D \simeq 0.5$; and the latest occurs at $z/D \simeq 2$ for $M_j = 1.35$. Downstream of some location, the hydrodynamic wave overcomes the acoustic, and the slope of the curve turns positive. This slope inversion is not visible for the case $M_j = 1.50$, which must be considered jointly with the shape of the wavenumber spectrum in figure 6(*j*): the $M_j = 1.50$ jet is the only case exhibiting a higher peak in negative wavenumber than in positive, which means a predominant upstream-propagating contribution. This observation is currently not understood. The second feature common to all cases is the wavy shape of the curve, resulting from the interaction between the instability wave, the acoustic wave and the shock cell pattern as discussed in § 3.1, with more details in Panda (1999). In addition to the hydrodynamic wave, the acoustic feedback is represented in figure 12 by a dashed line of negative slope $-\omega_s/c_0$ plotted from the point at which the hydrodynamic wave crosses the shock recognised as the acoustic

source. The modulation prevents the hydrodynamic wave from being localised with precision, but the latter is assumed to go along the line of best fit, calculated from the data between $z_N - L_{sc}/2$ and $z_N + L_{sc}/2$. The shock oscillation during a screech cycle (Panda 1998; André *et al.* 2011*b*) should also be considered. The amplitude of shock motion is estimated from the profile of $g(0.50D, z, t)$ fluctuations. Locations affected by the passage of the shock show the significantly largest level of fluctuations. The full width at half maximum of the peak associated with shock passage is considered as a reasonable estimation of the uncertainty of shock position, and is turned into a phase error.

The acoustic wave reaches the nozzle at the phase ϕ_{loop} expected to be a multiple of 2π. For all cases, ϕ_{loop} is indeed found to be close to an even multiple of π. The largest difference is 0.5π away from a 2π multiple, and all are positive. Although the modulation may play a role in these discrepancies, it might also be connected to an observation by Mitchell, Honnery & Soria (2012) in a comparable feedback process. Their experimental results point out the generation of an incited vortex ring in the mixing layer $0.25D$ downstream from the nozzle, suggesting that the trigger position of the instability could be slightly shifted. Phase ϕ_{loop} is considered to determine the number of screech cycles that compose the full screech loop, and to check for consistency between cases of the same mode.

The acoustic feedback is not expected to travel inside the mixing layer wherein convection slows down retrograde acoustics. The present model may underestimate the propagation time from the source to the nozzle. A pessimistic upper bound of the error is estimated by calculating the time spent by an acoustic wave to cross the shear layer half-thickness. This corresponds for the worst case $M_j = 1.15$ to a phase increment of 0.4π. Nevertheless this additional phase will not introduce ambiguity in defining the closest 2π multiple from ϕ_{loop}.

Cases $M_j = 1.07$, 1.10 and 1.13 are all the A1 mode, the acoustic source is located at the fourth shock tip, and the screech loop is made of four screech periods. Case $M_j = 1.15$ is the A2 mode; it differs from A1 by the number of screech periods in a loop – it is made of five periods. Higher-Mach-number jets all exhibit a flapping mode: $M_j = 1.23$, 1.37 and 1.45 emit acoustic from the third shock tip and their loops are composed of three periods, whereas $M_j = 1.32$ and 1.35 generate acoustic from the fourth shock tip and their loops are made of four periods. According to the Mach number of these different cases, the first set could show the characteristics of the b mode defined by Powell as a secondary mode (Powell *et al.* 1992), and the second set could be representative of the B mode. Nevertheless, Powell described secondary modes as modes coexisting with a dominant one – the b mode coexists with the A2 and C modes – but all the present cases manifest a single screech tone, and the C mode is not observed.

The convective velocity $\overline{U_c}$ averaged between the nozzle and the source at $z = z_N$ is deduced from the phase at the source ϕ_N by the relation

$$\overline{U_c} = f_s \frac{2\pi}{\phi_N} z_N. \tag{5.2}$$

The average shock cell length $\overline{L_{sc}}$ is calculated by

$$\overline{L_{sc}} = \frac{z_N}{N}. \tag{5.3}$$

Those results are summarised in table 5 and the convective velocity estimated from the wavenumber analysis is repeated for comparison. To better show the sensitivity of
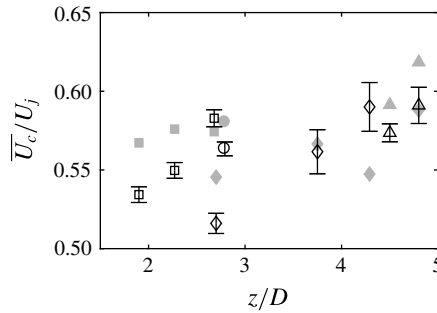
FIGURE 13. Spatially averaged convective velocity from the nozzle to the acoustic source normalised by the jet fully expanded velocity $\overline{U_c}/U_j$, against the acoustic source location z_N: □, A1 mode; ○, A2 mode; ◇, b mode; △, B mode; filled markers are from the wavenumber analysis; empty markers are from the phase analysis.

the convective velocity to Φ_s, error bars have been determined. They correspond either to the uncertainty linked to the shock motion, or to a floor of $\pm 0.05\pi$ representing the unknown third digit of Φ_s. The convective velocities estimated by the two methods are very close. The worst comparison concerns the cases $M_j = 1.07$ and $M_j = 1.45$; their convective velocities from wavenumber analysis differ respectively by -8% and $+7\%$ from phase evolution analysis. The good agreement between the results from the two different methods provides confidence for the interpretation of these figures. The main feature to be noted is the evolution of the convective velocity within a given mode – a fixed convective velocity cannot be attributed to a mode. The convective velocities are presented in figure 13 against the source location. Looking, for instance, at results for the mode A1, the convective velocity tends to rise when the position of the source is shifted downstream. This phenomenon is expected from the wavenumber analysis showing that the convective velocity is found close to $0.6U_j$ upstream of the source, and close to $0.7U_j$ downstream, so the convective velocity of the screech instability wave increases along its travel within the mixing layer. This can also explain why, with the exception of the $M_j = 1.13$ and $M_j = 1.45$ cases, all velocities calculated from wavenumber analysis are found to be higher than those from a phase analysis. The result of the spatial Fourier transform is somehow weighted by the local amplitude of the instability wave that grows along its travel within the mixing layer. The contribution coming from the region of low speed near the nozzle is underestimated in comparison with the influence of the high-convective-speed region near the source, resulting in an overestimation of the velocity averaged between the nozzle and the source. The convective velocity of the case $M_j = 1.23$ is equal to $0.52U_j$, against $0.56U_j$ for the case $M_j = 1.15$. However, the sources of these two cases are located very close to each other. The noticeable difference of U_c results from mode switching. It could also result from a compressibility effect due to the change of Mach number. Nevertheless, convective velocities are very similar for the two jets whose sources are located at $z/D = 4.6$ and $z/D = 4.7$, but whose Mach numbers are $M_j = 1.35$ and $M_j = 1.50$. In this case, the convective velocity seems not to be affected by compressibility effects. The mean convective velocity $\overline{U_c}$ is an input in screech frequency prediction models; therefore improving the screech frequency prediction requires a better understanding of the evolution of convective velocity with axial distance.

6. Conclusion

Acoustic and hydrodynamic properties of screech are investigated over 10 underexpanded supersonic jets of Mach number ranging from 1.07 to 1.50. Near-field acoustic measurements are achieved and schlieren visualisations of the jet near field and the shear layer are recorded. The two stages of the screech cycle that set the screech period are examined, namely the convection of the instability wave within the jet shear layer and the acoustic feedback. If it seems reasonable to consider the speed of sound as a constant along the feedback path, it is not the case for the convective velocity of the instability wave. The spatial dependence of U_c might involve a difficulty in predicting screech frequency; this velocity must be seen as an averaged value. Such an averaging must be calculated on a given spatial domain, which is bounded by the nozzle on one side and the screech acoustic source on the other side. The localisation of the source is therefore a major concern in understanding the screech loop and in predicting the screech frequency. An examination of the spatial evolution of the phase at the screech frequency of pressure signals has been conducted. The axial phase evolution survey provides the location of the source. It is found at the fourth shock tip for modes A1 and A2, and at either the third or the fourth shock tip for the B mode. The phase at the screech frequency is also measured within the shear layer from the schlieren records. In this region, the hydrodynamic contribution overcomes the acoustic, and, since the location of the source has been found, the convective velocity can be estimated by looking at the time spent by the instability wave to travel from the nozzle to the source. Its value varies from $0.54U_j$ to $0.61U_j$ with a tendency to rise when the distance between the nozzle and the source is increased.

Wavenumber spectra are also computed from the Fourier coefficients at the screech frequency of the schlieren data calculated along axially oriented lines. When considering results obtained upstream of the source, two peaks are identified in the spectra: one corresponds to the instability wave propagation, and the other to the acoustic feedback. The convective velocity is also estimated from these results, and is found to be in good agreement with the results obtained from the first method. The acoustic feedback wave propagation speed is estimated to be at $\pm 10\%$ of the speed of sound.

The screech loop is finally examined by measuring the phase of the screech-associated wave along the mixing layer down to the source, and by considering a feedback straight to the nozzle at the speed of sound. The time taken to travel the full loop is found to be equal to four periods for the A1 mode, five periods for the A2 mode, and either three or four periods for the B mode.

Appendix

The real part of the Fourier transform at the screech frequency is calculated at all pixels of the schlieren films and normalised in amplitude. The results are
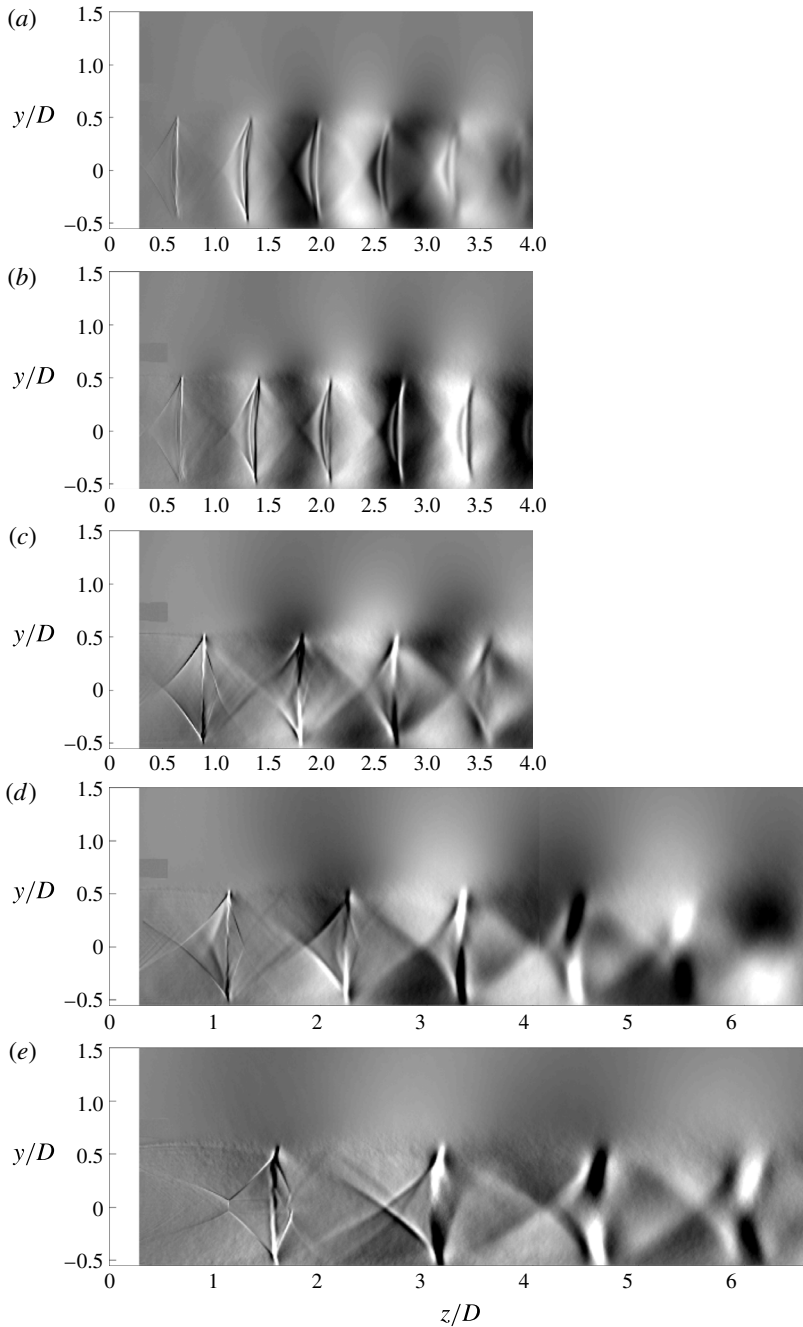
FIGURE 14. Real part of the Fourier transform at the screech frequency calculated from schlieren films: (*a*) $M_j = 1.13$ mode A1, (*b*) $M_j = 1.15$ mode A2, (*c*) $M_j = 1.23$ mode b, (*d*) $M_j = 1.32$ mode B, (*e*) $M_j = 1.50$ mode b. Results from two schlieren records are juxtaposed in (*d*) and (*e*).

provided in figure 14. Axisymmetric modes A1 and A2 are respectively represented in figure 14(*a*,*b*). Antisymmetric modes b and B are shown in figure 14(*c*,*e*) and figure 14(*d*). An azimuthal modal decomposition has been performed from the

signals of an azimuthal array of nine microphones following the method proposed in Massey & Ahuja (1997), and showed that all antisymmetric modes are flapping (B and b modes).

REFERENCES

ANDRÉ, B. 2011 Nozzle geometry. Available at: http://acoustique.ec-lyon.fr/jetnoise_uk.php.

ANDRÉ, B. 2012 Etude expérimentale de l'effet du vol sur le bruit de choc de jets supersoniques sous-détendus. PhD thesis, No. 2012-42, Ecole Centrale de Lyon.

ANDRÉ, B., CASTELAIN, T. & BAILLY, C. 2011a Experimental study of flight effects on screech in underexpanded jets. *Phys. Fluids* **23** (12), 126102.

ANDRÉ, B., CASTELAIN, T. & BAILLY, C. 2011b Shock-tracking procedure for studying screech-induced oscillations. *AIAA J.* **49** (7), 1563–1566.

BAILLY, C. & FUJI, K. 2016 High-speed jet noise. *Mech. Engng Rev.* **3** (1), 1–13.

BERLAND, J., BOGEY, C. & BAILLY, C. 2007 Numerical study of screech generation in a planar supersonic jet. *Phys. Fluids* **19** (7), 075105.

CHATTERJEE, A., GHODAKE, D. & SINGH, A. 2009 Screech frequency prediction in underexpanded axisymmetric screeching jets. *Intl J. Aeroacoust.* **8** (5), 499–510.

CLEM, M. M., ZAMAN, K. B. M. Q. & FAGAN, A. F. 2016 Variation of shock-spacing during screech stage-jumps. *Intl J. Aeroacoust.* **15** (3), 324–335.

DAVIES, M. G. & OLDFIELD, D. E. S. 1962 Tones from a choked axisymmetric jet. II. The self excited loop and mode of oscillation. *Acustica* **12** (4), 267–277.

EDGINGTON-MITCHELL, D., HONNERY, R. D. & SORIA, J. 2015 Staging behaviour in screeching elliptical jets. *Intl J. Aeroacoust.* **14** (7–8), 1005–1024.

EDGINGTON-MITCHELL, D., OBERLEITHNER, K., HONNERY, D. R. & SORIA, J. 2014 Coherent structure and sound production in the helical mode of a screeching axisymmetric jet. *J. Fluid Mech.* **748**, 822–847.

GAO, J. H. & LI, X. D. 2010 A multi-mode screech frequency prediction formula for circular supersonic jets. *J. Acoust. Soc. Am.* **127** (3), 1251–1257.

GASIOR, M. & GONZALEZ, J. L. 2004 Improving FFT frequency measurement resolution by parabolic and Gaussian spectrum interpolation. *AIP Conf. Proc.* **732** (1) 276–285.

GOJON, R., BOGEY, C. & MARSDEN, O. 2015 Large-eddy simulation of underexpanded round jets impinging on a flat plate 4 to 9 radii downstream from the nozzle. *AIAA Paper* 2210-2015.

HARPER-BOURNE, M. & FISHER, M. J. 1973 The noise from shock waves in supersonic jets. *AGARD CP* 131.

MASSEY, K. C. & AHUJA, K. K. 1997 Screech frequency prediction in light of mode detection and convection speed measurements for heated jets. *AIAA Paper* 97-1625.

MERCIER, B., CASTELAIN, T. & BAILLY, C. 2016 A schlieren and nearfield acoustic based experimental investigation of screech noise sources. *AIAA Paper* 2016-2799.

MERLE, M. 1957 Nouvelles recherches sur les fréquences ultrasonores émises par les jets d'air. *Annales des Télécommunications* **12** (12), 424–426.

MITCHELL, D., HONNERY, D. R. & SORIA, J. 2012 The visualization of the acoustic feedback loop in impinging underexpanded supersonic jet flows using ultra-high frame rate schlieren. *J. Vis.* **15** (4), 333–341.

NORUM, T. D. 1983 Screech suppression in supersonic jets. *AIAA J.* **21** (2), 235–240.

PANDA, J. 1996 An experimental investigation of screech noise generation. *AIAA Paper* 96-1718.

PANDA, J. 1998 Shock oscillation in underexpanded screeching jets. *J. Fluid Mech.* **363**, 173–198.

PANDA, J. 1999 An experimental investigation of screech noise generation. *J. Fluid Mech.* **378**, 71–96.

PANDA, J. & RAMAN, G. 1997 Underexpanded screeching jets from circular, rectangular, and elliptic nozzles. *AIAA Paper* 97-1623.

PONTON, M. K. & SEINER, J. M. 1995 Acoustic study of b helical mode for choked axisymmetric nozzle. *AIAA J.* **33** (3), 413–420.

POWELL, A. 1953 On edge tones and associated phenomena. *Acustica* **3**, 233–243.

POWELL, A., UMEDA, Y. & ISHII, R. 1990 The screech of round choked jets, revisited. *AIAA Paper* 90-3980.

POWELL, A., UMEDA, Y. & ISHII, R. 1992 Observations of the oscillation modes of choked circular jets. *J. Acoust. Soc. Am.* **92** (5), 2823–2836.

RAMAN, G. 1997 Cessation of screech in underexpanded jets. *J. Fluid Mech.* **336**, 69–90.

RAMAN, G. 1999 Supersonic jet screech: half-century from Powell to the present. *J. Sound Vib.* **225** (3), 543–571.

SHARIFF, K. & MANNING, T. A. 2013 A ray tracing study of shock leakage in a model supersonic jet. *Phys. Fluids* **25** (7), 076103.

SHEN, H. & TAM, C. K. W. 2002 Three-dimensional numerical simulation of the jet screech phenomenon. *AIAA J.* **40** (1), 33–41.

SUZUKI, T. & LELE, S. K. 2003 Shock leakage through an unsteady vortex-laden mixing layer: application to jet screech. *J. Fluid Mech.* **490**, 139–167.

TAM, C. K. W. 1995 Supersonic jet noise. *Annu. Rev. Fluid Mech.* **27** (1), 17–43.

TAM, C. K. W., JACKSON, J. A. & SEINER, J. M. 1985 A multiple-scales model of the shock-cell structure of imperfectly expanded supersonic jets. *J. Fluid Mech.* **153**, 123–149.

TAM, C. K. W., PARRISH, S. A. & VISWANATHAN, K. 2014 Harmonics of jet screech tones. *AIAA J.* **52** (11), 2471–2479.

TAM, C. K. W., SEINER, J. M. & YU, J. C. 1986 Proposed relationship between broadband shock associated noise and screech tones. *J. Sound Vib.* **110** (2), 309–321.

UMEDA, Y. & ISHII, R. 2001 On the sound sources of screech tones radiated from choked circular jets. *J. Acoust. Soc. Am.* **110** (4), 1845–1858.

VELTIN, J., DAY, J. B. & MCLAUGHLIN, K. D. 2011 Correlation of flowfield and acoustic field measurements in high-speed jets. *AIAA J.* **49** (1), 150–163.

VELTIN, J. & MCLAUGHLIN, D. K. 2008 Noise mechanisms investigation in shock containing screeching jets using optical deflectometry. *AIAA Paper* 2008-2889.

WESTLEY, R. & WOOLLEY, J. H. 1969 The near field sound pressures of a choked jet during a screech cycle. *AGARD CP* **42**, 23.1–23.13.